

SN 2018gk Revisited: the Photosphere, the Central Engine, And the Putative Dust

TAO WANG (王涛),¹ SHAN-QIN WANG (王善钦),¹ WEN-PEI GAN (甘文沛),² AND LONG LI (李龙)³

¹*Guangxi Key Laboratory for Relativistic Astrophysics, School of Physical Science and Technology, Guangxi University, Nanning 530004, China*

²*Nanjing Institute of Astronomical Optics & Technology, Nanjing 210042, China*

³*Department of Astronomy, School of Physical Sciences, University of Science and Technology of China, Hefei 230026, China*

ABSTRACT

In this paper, we perform a comprehensive study for the physical properties of SN 2018gk which is a luminous type IIb supernova (SN). We find that the early-time photospheric velocity vary from a larger value to a smaller value before the photosphere reach a temperature floor. We generalize the photosphere modulus and fit the multiband light curves (LCs) of SN 2018gk. We find that the ⁵⁶Ni mass model require $\sim 0.90 M_{\odot}$ of ⁵⁶Ni which is larger than the derived ejecta mass ($\sim 0.10 M_{\odot}$). Alternatively, we use the magnetar plus ⁵⁶Ni and the fallback plus ⁵⁶Ni models to fit the LCs of SN 2018gk, finding that the two models can fit the LCs. We favor the magnetar plus ⁵⁶Ni since the parameters are rather reasonable ($M_{\text{ej}} = 1.65 M_{\odot}$, $M_{\text{Ni}} = 0.05 M_{\odot}$ which is smaller than the upper limit of the value of the ⁵⁶Ni mass can by synthesized by the neutrino-powered core collapse SNe $B = 6.52 \times 10^{14}$ G which is comparable to those of luminous and superluminous SNe studied in the literature, and $P_0 = 10.42$ ms which is comparable to those of luminous SNe), while the validity of the fallback plus ⁵⁶Ni model depends on the accretion efficiency (η). Therefore, we suggest that SN 2018gk might be a SN IIb mainly powered by a central engine. Finally, we confirm the NIR excesses of the SEDs of SN 2018gk at some epochs and constrain the physical properties of the putative dust using the blackbody plus dust emission model.

Keywords: Supernovae; Type II supernovae; Magnetars; Circumstellar dust

1. INTRODUCTION

It is widely believed that massive stars whose zero-age main-sequence mass M_{ZAMS} are $\gtrsim 8.0 M_{\odot}$ would explode as core-collapse supernovae (CCSNe; Woosley et al. 2002), leaving neutron star (NSs) or black hole (BHs). Most CCSNe can be classified into types IIP, IIL, IIn, IIb, Ib, and Ic according to the spectra and light curves (LCs) (Filippenko 1997). In the past two decades, some new sub-classes of CCSNe, such as Ibn and Icn, are confirmed. In general, SNe Ib, Ic, IIb, Ibn, and Icn can be collectively referred to as stripped-envelope SNe (SESNe; Clocchiatti et al. 1996), since the hydrogen and/or helium envelopes of their progenitors were partly or completely stripped.

The early-time spectra of SNe IIb show hydrogen absorption lines, while their late-time spectra do not show hydrogen lines, but show helium absorption lines (Filippenko 1988). These features make SNe IIb to be the transitional type between SNe II whose spectra continue to show hydrogen absorption lines and SNe Ib whose spectra have helium absorption lines. It is suggested that the progenitors stars of SNe IIb lost most of hydrogen envelopes through stellar wind and/or binary interactions (Podsiadlowski et al. 1992; Sravan et al. 2019; Yoon et al. 2010, 2017), leaving $\sim 0.1 M_{\odot}$ of hydrogen envelopes.

The peak absolute magnitudes (M_{peak}) of most SNe IIb is dimmer than -19.0 mag. However, there are few SNe IIb are overluminous, with M_{peak} brighter than -19.0 mag or even -20.0 mag which are between those of superluminous supernovae (SLSNe, $M_{\text{peak}} \lesssim -21$ mag, Gal-Yam 2012) and normal SNe.¹ For instance, the M_{peak} of

Corresponding author: Shan-Qin Wang (王善钦)
shanqinwang@gxu.edu.cn

¹ We note that, however, luminous SNe with M_{peak} being -20 to -21 mag are also classified to be SLSNe in some literature.

SNe I Ib PTF10hgi, DES14X2fna, and SN 2018gk (ASASSN-18am) are ~ -20.42 mag (g - band, [Inserra et al. 2013](#))², ~ -19.3 mag (g - band, [Grayling et al. 2021](#)), and ~ -19.7 mag (V - band, [Bose et al. 2021](#), hereafter B21), respectively.

This work focuses on the physical properties of SN 2018gk. SN 2018gk was discovered ([Brimacombe, Stone & Stanek 2018](#)) by the All-Sky Automated Survey for Supernovae (ASASSN; [Shappee et al. 2014](#); [Kochanek et al. 2017](#)) on 2018 January 12.5 UT. The host galaxy of SN 2018gk is WISE J163554.27+400151.8 whose redshift z is 0.031010 ± 0.000005 ([SDSS Collaboration 2017](#)). The spectra sequence of SN 2018gk indicate that it is an SN I Ib. B21 find that its M_{peak} in V -band is ≈ -19.7 mag, which is at least one magnitude brighter than those of most SNe I Ib, and comparable to those of luminous SNe I Ib PTF10hgi and DES14X2fna.

B21 construct the bolometric LC and use the radiative diffusion (^{56}Ni plus internal energy) model to fit it, finding that the required ^{56}Ni mass M_{Ni} is $\sim 0.4 M_{\odot}$. They also use the magnetar plus ^{56}Ni model to fit the bolometric LC and find that the initial period (P_0) and the magnetic field strength (B) of the magnetar are ~ 1.2 ms and $\sim 4 \times 10^{15}$ G, respectively. As pointed out by B21, the value of B is higher than those of SLSNe I modeled by [Nicholl et al. \(2017\)](#) which are a few 10^{13} G to a few 10^{14} G. B21 suggest that the extreme value of B , together with the very short P_0 would extract rotational energy of up to $\sim 10^{52}$ erg in the first 10 s after the explosion, thus significantly affecting SN shock dynamics. Furthermore, B21 point out that the magnetar do not significantly reduce M_{Ni} since the ^{56}Ni mass derived by the magnetar plus ^{56}Ni model is $\sim 0.3 M_{\odot}$. The ^{56}Ni masses derived by the two models are larger than the upper limit ($\sim 0.2 M_{\odot}$) of the ^{56}Ni mass that can be synthesized by neutrino-power mechanism ([Sukhbold et al. 2016](#); [Ertl et al. 2020](#)). [Soker & Kaplan \(2021\)](#) fit the V - band data of SN 2018gk using a two-components bipolar model. The photometry in all other bands have not been used.

Therefore, we suggest that the energy source of SN 2018gk is still elusive and deserve further study. In this paper, we research the energy source model, the physical parameters of the models as well as the properties of the possible dust of SN 2018gk. In Section 2, we model the multi-band LCs for SN 2018gk using three models (the ^{56}Ni model, the magnetar plus ^{56}Ni model, and the fallback plus ^{56}Ni model). In Section 3, we study the NIR excesses of SN 2018gk and constrain the physical properties of the putative dust. In Section 4, we discuss our results. We draw some conclusions in Section 5. Throughout the paper, we assume $\Omega_m = 0.315$, $\Omega_{\Lambda} = 0.685$, and $H_0 = 67.3 \text{ km s}^{-1} \text{ Mpc}^{-1}$ ([Planck Collaboration 2014](#)). The values of the Milky Way reddening (E_{B-V}) from [Schlafly & Finkbeiner \(2011\)](#).

2. MODELING THE MULTI-BAND LIGHT CURVES OF SN 2018GK

B21 construct and fit the bolometric LC of SN 2018gk. It should be noted that, however, the upper limits at two very early epochs in V - band and six data in V - and g - bands at four early epochs cannot be included in the constructed LC. Therefore, modeling the multi-band LCs might get more reliable results and pose more stringent constraints on the physical properties of SN 2018gk.

The bolometric luminosity of SNe powered is (see e.g., [Arnett 1982](#); [Chatzopoulos et al. 2012](#); [Wang et al. 2015](#); [Wang & Gan 2022](#))

$$L_{\text{SN}}(t) = \frac{2}{\tau_m} e^{-\frac{t^2}{\tau_m^2}} \int_0^t e^{\frac{t'^2}{\tau_m^2}} \frac{t'}{\tau_m} L_{\text{input}}(t') \left(1 - e^{-\tau_{\gamma(e^+)}(t)}\right) dt', \quad (1)$$

here, $\tau_m = (2\kappa M_{\text{ej}}/\beta_{\text{SN}} v_{\text{sc}} c)^{1/2}$ is the diffusion timescale ([Arnett 1982](#)), κ is the optical opacity of the ejecta which is usually assumed to be $0.05 - 0.20 \text{ cm}^2 \text{ g}^{-1}$, M_{ej} is the SN ejecta mass, v_{sc} is the scale velocity of the SN ([Arnett 1982](#)), c is the speed of light, $\beta_{\text{SN}} \simeq 13.8$ is a constant ([Arnett 1982](#)); $\tau_{\gamma(e^+)}(t) = t_{0,\gamma(e^+)}/t^2$ is the optical depth to γ -rays ([Chatzopoulos et al. 2009, 2012](#)) or positrons, $\kappa_{\gamma,\text{Ni}}$ and κ_{e^+} are respectively the opacity of the γ -rays from ^{56}Ni cascade decay and the positron from ^{56}Co decay, $t_{0,\gamma(e^+)} = (3\kappa_{\gamma(e^+)} M_{\text{ej}}/4\pi v^2)^{1/2}$ is γ -ray (positron) trapping parameter; $L_{\text{input}}(t)$ is the power function of the energy source(s).

As multi-band LC fitting is used, a model must be included for the spectral energy distributions (SEDs). The SEDs of the SNe can be described by the UV absorbed blackbody model ([Nicholl et al. 2017](#); [Prajs et al. 2017](#)),

$$F_{\nu} = \begin{cases} \left(\frac{\lambda}{\lambda_{\text{CF}}}\right)^{\beta'} (2\pi h\nu^3/c^2) (e^{\frac{h\nu}{k_b T_{\text{ph}}}} - 1)^{-1} \frac{R_{\text{ph}}^2}{D_L^2}, & \lambda \leq \lambda_{\text{CF}} \\ (2\pi h\nu^3/c^2) (e^{\frac{h\nu}{k_b T_{\text{ph}}}} - 1)^{-1} \frac{R_{\text{ph}}^2}{D_L^2}, & \lambda > \lambda_{\text{CF}} \end{cases} \quad (2)$$

² PTF10hgi had been classified to be a type Ic SLSN [Inserra et al. \(2013\)](#), but [Quimby et al. \(2018\)](#) suggest that it is an SLSN I Ib, since its spectrum shows clear evidence of hydrogen and helium.

T_{ph} is the temperature of the SN photosphere, R_{ph} is the radius of the SN photosphere, D_{L} is the luminosity distance of the SN, λ_{CF} is the cutoff wavelength, β' is a dimensionless free parameter (Yan et al. 2020).

In general, the photosphere evolution can be described by Nicholl et al. (2017) which assumes that the early photosphere expansion velocity (v_{ph}) of SNe is constant and the late-time temperature is a constant (T_{f}). We find, however, that the curve of early photosphere expansion velocity can be divided into two episodes having different velocities (v_{ph1} and v_{ph2} , see the green dash-dotted line and the red dashed line of Figure 1). The transition time when v_{ph1} became v_{ph2} is denoted as t_{tr} which is respective to the time of the first photometry (see the orange vertical dotted line of Figure 1). The time interval between the explosion date and the the time when v_{ph1} became v_{ph2} (t_1) is $t_{\text{tr}} - t_{\text{shift}}$; here, t_{shift} is the explosion time relative to the first photometry. Therefore, we generalize the photosphere modulus as follow,

$$R_{\text{ph}}(t) = \begin{cases} v_{\text{ph1}}t, & t \leq t_1 \quad \text{and} \quad \left(\frac{L_{\text{SN}}(t)}{4\pi\sigma(v_{\text{ph1}}t)^2}\right)^{\frac{1}{4}} > T_{\text{f}} \\ v_{\text{ph1}}t_1 + v_{\text{ph2}}(t - t_1), & t > t_1 \quad \text{and} \quad \left(\frac{L_{\text{SN}}(t)}{4\pi\sigma(v_{\text{ph1}}t_1 + v_{\text{ph2}}t)^2}\right)^{\frac{1}{4}} > T_{\text{f}} \\ \left(\frac{L(t)}{4\pi\sigma T_{\text{f}}^4}\right)^{\frac{1}{2}}, & \left(\frac{L(t)}{4\pi\sigma(v_{\text{ph1}}t_1 + v_{\text{ph2}}t)^2}\right)^{\frac{1}{4}} \leq T_{\text{f}} \end{cases} \quad (3)$$

$$T_{\text{ph}}(t) = \begin{cases} \left(\frac{L_{\text{SN}}(t)}{4\pi\sigma v_{\text{ph1}}^2 t^2}\right)^{\frac{1}{4}}, & t \leq t_1 \quad \text{and} \quad \left(\frac{L_{\text{SN}}(t)}{4\pi\sigma(v_{\text{ph1}}t)^2}\right)^{\frac{1}{4}} > T_{\text{f}} \\ \left(\frac{L_{\text{SN}}(t)}{4\pi\sigma(v_{\text{ph1}}t_1 + v_{\text{ph2}}t)^2}\right)^{\frac{1}{4}}, & t > t_1 \quad \text{and} \quad \left(\frac{L_{\text{SN}}(t)}{4\pi\sigma(v_{\text{ph1}}t_1 + v_{\text{ph2}}t)^2}\right)^{\frac{1}{4}} > T_{\text{f}} \\ T_{\text{f}}, & \left(\frac{L(t)}{4\pi\sigma(v_{\text{ph1}}t_1 + v_{\text{ph2}}t)^2}\right)^{\frac{1}{4}} \leq T_{\text{f}} \end{cases} \quad (4)$$

2.1. Modeling the multi-band LCs of SN 2018gk using the ^{56}Ni model

We first fit the multi-band LCs of SN 2018gk using the the ^{56}Ni model. Throughout this paper, v_{sc} is assumed to be v_{ph1} . To include the energy deposited by γ -rays and positrons, we adopt a more complicated equation below (see, e.g., Valenti et al. 2008)

$$L_{\text{input}}(t) \left(1 - e^{-\tau_{\gamma}(e^+)(t)}\right) = S^{\text{Ni}}(\gamma) + S^{\text{Co}}(\gamma) + S_{e^+}^{\text{Co}}(\gamma) + S_{e^+}^{\text{Co}}(\text{KE}) \quad (5)$$

here, $S^{\text{Ni}}(\gamma) = \epsilon_{\text{Ni}} M_{\text{Ni}} e^{-t/\tau_{\text{Ni}}} (1 - e^{-\tau_{\gamma}(t)})$ is the source energy of the ^{56}Ni decay, M_{Ni} is the initial mass of ^{56}Ni ; $\epsilon_{\text{Ni}} = 3.9 \times 10^{10} \text{ erg s}^{-1} \text{ g}^{-1}$ (Cappellaro et al. 1997; Sutherland & Wheeler 1984) is the energy generation rate of ^{56}Ni , $\tau_{\text{Ni}} = 8.8$ days is the lifetime of the ^{56}Ni ; $S^{\text{Co}}(\gamma) = 0.81 \mathcal{E}_{\text{Co}} (1 - e^{-(t_0, \gamma/t)^2})$, $S_{e^+}^{\text{Co}}(\gamma) = 0.164 \mathcal{E}_{\text{Co}} (1 - e^{-(t_0, \gamma/t)^2}) (1 - e^{-(t_0, e^+/t)^2})$, and $S_{e^+}^{\text{Co}}(\text{KE}) = 0.036 \mathcal{E}_{\text{Co}} (1 - e^{-(t_0, e^+/t)^2})$ are respectively the source energy of the ^{56}Co decay, the energy deposited by the γ -rays produced in the positron annihilation, and the source energy due to the kinetic energy of the positrons (Valenti et al. 2008), where $\mathcal{E}_{\text{Co}} = \epsilon_{\text{Co}} M_{\text{Ni}} e^{-t/\tau_{\text{Co}}} - e^{-t/\tau_{\text{Ni}}}$ is the rate of energy production by the ^{56}Co decay, $\epsilon_{\text{Co}} = 6.8 \times 10^9 \text{ erg s}^{-1} \text{ g}^{-1}$ (Maeda et al. 2003) is the energy generation rate of ^{56}Co , $\tau_{\text{Co}} = 111.3$ days is the lifetime of ^{56}Co .

By combining Equations 1, 2, 3, 4, and 5, we can construct the ^{56}Ni model used to fit the multi-band LCs of SN 2018gk. Considering the fact that the rise time is rather short, we fixed the value of κ to be $0.05 \text{ cm}^2 \text{ g}^{-1}$ throughout this paper to obtain a relative larger ejecta mass. The definitions, the units, and the priors of the parameters of the ^{56}Ni model are listed in Table 1. We note that $\kappa_{\gamma, \text{Ni}}$ and κ_{e^+} are also free parameters in our model.³

The Markov Chain Monte Carlo (MCMC) using the `emcee` Python package (Foreman-Mackey et al. 2013) is adopted to get the best-fitting parameters and the $1\text{-}\sigma$ range of the parameters. We employ 20 walkers, each walker runs 30,000 steps for the ^{56}Ni model. The $1\text{-}\sigma$ uncertainties are corresponding to the 16th and 84th percentiles of the posterior samples.

³ It is believed that the value of $\kappa_{\gamma, \text{Ni}}$ is determined by the γ -ray energy E_{γ} (0.314 and 0.814 MeV for ^{56}Ni decay to ^{56}Co and then to ^{56}Fe) and the number of baryons per electron Y_e (~ 0.5). Swartz et al. (1995) find MCMC that $\kappa_{\gamma, \text{Ni}}$ is about $0.06_{-0.01}^{+0.01} Y_e$ at $E_{\gamma} > 0.1$ MeV. Therefore, $\kappa_{\gamma, \text{Ni}}$ is usually set to be $0.027 \text{ cm}^2 \text{ g}^{-1}$ (e.g., Cappellaro et al. 1997; Maeda et al. 2003; Mazzali et al. 2000). However, there is evidence that $\kappa_{\gamma, \text{Ni}}$ of some SNe has larger values. For instance, based on the parameters derived by Nagy & Vinkó (2016) for SN 1987A ($A_g = 2.7 \times 10^5 \text{ day}^2$, $M_{\text{ej}} = 8.6 M_{\odot}$, $E_k = 1.17 \times 10^{51} \text{ erg}$), we find that $\kappa_{\gamma, \text{Ni}} \sim 0.11 \text{ cm}^2 \text{ g}^{-1}$. So we assume $\kappa_{\gamma, \text{Ni}}$ is a free parameter whose lower limit is $0.027 \text{ cm}^2 \text{ g}^{-1}$. The values of κ_{e^+} are usually set to be $7 \text{ cm}^2 \text{ g}^{-1}$ or $10 \text{ cm}^2 \text{ g}^{-1}$ (Milne et al. 1999). Cappellaro et al. (1997) argued that $7 \text{ cm}^2 \text{ g}^{-1}$ is the best value of κ_{e^+} ; however, they derived this value based on the assumption that $\kappa_{\gamma, \text{Ni}}$ is $0.027 \text{ cm}^2 \text{ g}^{-1}$. We do not adopt this value, since $\kappa_{\gamma, \text{Ni}}$ is set to be a free parameter in this work. In fact, the value of κ_{e^+} depends on the value of the number of free electrons per nucleus χ_e (the ionization fraction, see, e.g., Milne et al. 1999): for $\chi_e = 0.01$, $\kappa_{e^+} = 4 \text{ cm}^2 \text{ g}^{-1}$; for $\chi_e = 3$, $\kappa_{e^+} = 14 \text{ cm}^2 \text{ g}^{-1}$. We assume that κ_{e^+} is also a free parameter whose lower limit and upper limit are $4 \text{ cm}^2 \text{ g}^{-1}$ and $14 \text{ cm}^2 \text{ g}^{-1}$, respectively.

The fit of the ^{56}Ni model is shown in Figure 2. The parameters and the corresponding corner plot are presented in Table 1 and Figure A1, respectively. The relevant parameters of the ^{56}Ni model are $M_{\text{ej}} = 0.10 M_{\odot}$, $t_{\text{tr}} = 14.02$ days, $v_{\text{ph1}} = 1.52 \times 10^9 \text{ cm s}^{-1}$, $v_{\text{ph2}} = 0.16 \times 10^9 \text{ cm s}^{-1}$, $M_{\text{Ni}} = 1.59 M_{\odot}$, $T_{\text{f}} = 4921.90 \text{ K}$, $t_{\text{shift}} = -1.76$ days (the offset of the best-fitting explosion epoch with respect to the explosion epoch adopted by B21 is 1.36 days), and $\kappa_{\gamma, \text{Ni}} = 0.35 \text{ cm}^2 \text{ g}^{-1}$. Using these parameters, we find that the value of γ -ray trapping parameter $t_{0, \gamma, \text{Ni}}$ is 31.25 days. We find that the derived ^{56}Ni mass ($1.59 M_{\odot}$) is significantly larger than the derived ejecta mass ($0.10 M_{\odot}$).

It should be noted that, however, Arnett (1982)'s model we adopt above might overestimate the ^{56}Ni masses of SESNe (including IIB). We therefore calculate the more accurate value of ^{56}Ni mass of SN 2018gk using the Equation derived by Khatami & Kasen (2019)

$$M_{\text{Ni}} = \frac{L_{\text{peak}} \beta^2 t_{\text{peak}}^2}{2 \epsilon_{\text{Ni}} \tau_{\text{Ni}}^2} \left(\left(1 - \frac{\epsilon_{\text{Co}}}{\epsilon_{\text{Ni}}} \right) \times \left(1 - (1 + \beta t_{\text{peak}} / \tau_{\text{Ni}}) e^{-\beta t_{\text{peak}} / \tau_{\text{Ni}}} \right) + \frac{\epsilon_{\text{Co}} \tau_{\text{Co}}^2}{\epsilon_{\text{Ni}} \tau_{\text{Ni}}^2} \left(1 - (1 + \beta t_{\text{peak}} / \tau_{\text{Co}}) e^{-\beta t_{\text{peak}} / \tau_{\text{Co}}} \right) \right)^{-1} \quad (6)$$

The value of β is ~ 0.78 for SNe IIB (Afsariardchi et al. 2021).

Using the peak luminosity (L_{peak}) and the rise time (t_{peak}) of the bolometric LC produced by the best-fitting parameters of the multi-band LC fit, we find that the M_{Ni} value derived by Equation 6 is $0.90 M_{\odot}$. While this value is lower than the value derived by Arnett (1982)'s model, it is significantly higher than the value of ^{56}Ni derived by B21 using the Katz, Kushnir & Dong (2013) integral method and is still larger than the mass of the eject. This indicate that the ^{56}Ni model cannot account for the LCs of SN 2018gk.

In Figure 3, we plot our synthesized bolometric LC of SN 2018gk, the power injection function curve derived from the parameters of B21 ($M_{\text{Ni}} = 0.43 M_{\odot}$, $t_{0, \gamma, \text{Ni}} = 53$ days), as well as the power injection function curve derived from our parameters ($M_{\text{Ni}} = 1.59 M_{\odot}$, $t_{0, \gamma, \text{Ni}} = 31.25$ days). For comparison, the curve derived from $M_{\text{Ni}} = 1.85 M_{\odot}$ and a infinite $t_{0, \gamma, \text{Ni}}$ is also plotted.

We find that both the curves derived by B21's parameters and our parameters can fit the late-time (>75 days) can match the synthesized bolometric LC, while the curve with infinite $t_{0, \gamma, \text{Ni}}$ cannot fit the bolometric LC. It should be noted that, however, the curve using the B21's parameters is much lower than the bolometric luminosity of the SN 2018gk around the peak, indicating that, in B21's two-component diffusion model, the early-time LC is (mainly) powered by the internal energy.

In fact, the ^{56}Ni masses derived from the peak luminosity of SLSNe and luminous SNe are usually significantly higher than those derived from the tails (except for the cases in which the SLSNe is pair instability SNe candidates), see, e.g., Table 3 of De Cia et al. (2018). The ^{56}Ni masses derived from tails are most reliable. Therefore, the peak luminosity of SLSNe and luminous SNe are usually assumed to be mainly powered by the energy sources (magnetar, ejecta-CSM interaction, fallback, or internal energy) rather than ^{56}Ni heating.

SN 2018gk is a luminous SN having observational properties similar to those of SLSNe and luminous SNe. The large discrepancy between the inferred ^{56}Ni masses derived from the peak (see above) and the tail (inferred by B21 using Katz, Kushnir & Dong 2013) is also indicative of the necessity of introducing another energy source to account for the luminous peak.

2.2. Modeling the multi-band LCs of SN 2018gk using the magnetar Plus ^{56}Ni model

Although B21 show that the two-component diffusion model taking the internal energy and ^{56}Ni heating can fit the bolometric LC of SN 2018gk, the derived ^{56}Ni mass ($\sim 0.43 M_{\odot}$) is higher than the upper limit ($\sim 0.2 M_{\odot}$) of the ^{56}Ni mass that can be synthesized by neutrino-power mechanism. To reduce the required ^{56}Ni , B21 use the magnetar plus ^{56}Ni model to fit the bolometric LC of SN 2018gk. They find that the model ^{56}Ni only slightly reduce the ^{56}Ni mass to $0.3 M_{\odot}$ which is still larger than $0.2 M_{\odot}$. Moreover, they find that the derived parameters of the magnetars are very extreme: the initial period (P_0) and the magnetic field strength (B) of the magnetar are $\sim 1.2 \text{ ms}$ and $\sim 4 \times 10^{15} \text{ G}$, respectively. These values are inconsistent with the typical values of the magnetars supposed to power the LCs of luminous SNe (see, e.g., Wang et al. 2015; Gomez et al. 2022) and SLSNe (see, e.g., Nicholl et al. 2017; Liu et al. 2017).

Hence, we check the magnetar plus ^{56}Ni model by fitting the LCs of SN 2018gk. The power function $L_{\text{input}}(t)$ of the magnetar we adopt is

$$L_{\text{input}}(t) = L_{\text{input, mag}}(t) = \frac{E_p}{\tau_p} \frac{1}{(1 + t/\tau_p)^2}, \quad (7)$$

where $E_p \simeq (1/2)I_{\text{mag}}\Omega_{\text{mag}}^2$ is the rotational energy of a magnetar, $\tau_p = 6I_{\text{mag}}c^3/B^2R_{\text{mag}}^6\Omega_{\text{mag}}^2$ is the spin-down timescale of the magnetar (Kasen & Bildsten 2010). $I_{\text{mag}} = (2/5)M_{\text{mag}}R_{\text{mag}}^2$ is the moment of inertia of a magnetar, $\Omega_{\text{mag}} = 2\pi/P_0$ is initial angular velocity (P_0 is initial period of the magnetar), B is the magnetic field strength of the magnetar. The mass (M_{mag}) and the radius (R_{mag}) of the magnetar are usually set to be $1.4 M_{\odot}$ and 10 km, respectively; using the two values, the canonical value of I_{mag} is $\sim 10^{45}$ g cm² (see, e.g., Woosley 2010). The γ -ray opacity κ_{γ} in Equation 1 become $\kappa_{\gamma,\text{mag}}$.

By combining Equations 1, 2, 3, 4, 5, and 7, the magnetar plus ⁵⁶Ni model can be constructed. The definitions, the units, and the priors of the parameters of the magnetar plus ⁵⁶Ni model are listed in Table 2. The MCMC using the `emcee` Python package is adopted to get the best-fitting parameters and the 1- σ range of the parameters. We employ 20 walkers, each walker runs 30,000 steps for the magnetar plus ⁵⁶Ni model. The 1- σ uncertainties are corresponding to the 16th and 84th percentiles of the posterior samples.

The fit of the magnetar plus ⁵⁶Ni model is shown in Figure 4. The parameters and the corresponding corner plot are presented in Table 2 and Figure A2, respectively. The relevant parameters of the magnetar plus ⁵⁶Ni model are $M_{\text{ej}} = 1.65 M_{\odot}$, $P_0 = 10.42$ ms, $B = 6.52 \times 10^{14}$ G, $M_{\text{Ni}} = 0.08 M_{\odot}$, $t_{\text{tr}} = 17.15$ days, $v_{\text{ph1}} = 1.07 \times 10^9$ cm s⁻¹, $v_{\text{ph2}} = 0.11 \times 10^9$ cm s⁻¹, $T_{\text{f}} = 5254.04$ K, $t_{\text{shift}} = -6.35$ days (the offset of the best-fitting explosion epoch with respect to the explosion epoch adopted by B21 is 5.95 days), $\kappa_{\gamma,\text{Ni}} = 0.19$ cm²g⁻¹ ($t_{0,\gamma,\text{Ni}} = 132.17$ days), and $\kappa_{\gamma,\text{mag}} = 0.028$ cm²g⁻¹ ($t_{0,\gamma,\text{mag}} = 50.83$ days).

We find that, using the same scenario (the magnetar plus ⁵⁶Ni), our derived P_0 (10.42 ms) is significantly larger than that (1.2 ms) of B21; our derived B (6.52×10^{14} G) is about 1/6 of that (4×10^{15} G) of B21. We suggest that the discrepancies between our values of B and P_0 and those of B21 might be due to the differences of explosion epoch and other parameters, since the large parameter space involved in the magnetar plus ⁵⁶Ni model might yield another parameter sets that can fit the same LCs. However, our derived values of B and P_0 are not extreme and comparable to those of luminous SNe studied in the literature, indicating that the magnetar plus ⁵⁶Ni model is reasonable.

Furthermore, our derived ⁵⁶Ni mass is $0.08 M_{\odot}$, which can be reduced by to $0.05 M_{\odot}$ by using Equation 6. This value is much lower than the ⁵⁶Ni mass derived by using the ⁵⁶Ni model, suggesting that the magnetar can effectively reduce the ⁵⁶Ni needed to power the LCs of SN 2018gk. More importantly, the derived ⁵⁶Ni is lower than the upper limit ($\sim 0.2 M_{\odot}$) of the ⁵⁶Ni mass that can be synthesized by neutrino-power mechanism, and comparable to the ⁵⁶Ni masses of typical SNe IIB⁴.

2.3. Modeling the multi-band LCs of SN 2018gk using the Fallback Plus ⁵⁶Ni model

The fallback and fallback plus ⁵⁶Ni models are also used to fit the multi-band LCs of some SNe (see, e.g., the references of B21 and Moriya et al. 2018). B21 disfavor the fallback model since the ⁵⁶Ni synthesized by the SN shock is accreted on to the central compact remnant and very low or no ⁵⁶Ni mass can survive. Here, we check the possibility that the multi-band LCs of SN 2018gk can be fitted by the fallback plus ⁵⁶Ni model.

The power function $L_{\text{input}}(t)$ of the fallback model is (Moriya et al. 2018).

$$L_{\text{input}}(t) = L_{\text{input,fb}}(t) = \begin{cases} L_1 (t_{\text{tr,fb}}/1 \text{ s})^{-5/3}, & t < t_{\text{tr,fb}} \\ L_1 (t/1 \text{ s})^{-5/3}, & t \geq t_{\text{tr,fb}} \end{cases} \quad (8)$$

where L_1 is a constant and $t_{\text{tr,fb}}$ is the transition time when the constant became a power-law function (Moriya et al. 2018).

By combining Equations 1, 2, 3, 4, 5, and 8, the fallback plus ⁵⁶Ni model can be constructed. The definitions, the units, and the priors of the parameters of the fallback plus ⁵⁶Ni model are listed in Table 3. The MCMC using the `emcee` Python package is adopted to get the best-fitting parameters and the 1- σ range of the parameters. We employ 20 walkers, each walker runs 30,000 steps for the fallback plus ⁵⁶Ni model. The 1- σ uncertainties are corresponding to the 16th and 84th percentiles of the posterior samples.

The fit of the fallback plus ⁵⁶Ni model is shown in Figure 5. The parameters and the corresponding corner plot are presented in Table 3 and Figure A3, respectively. We find that the LCs can be well fitted by the fallback plus ⁵⁶Ni model, although the LCs are rather narrow. The relevant parameters of the fallback plus ⁵⁶Ni model are $M_{\text{ej}} =$

⁴ Afsariardchi et al. (2021) derive the ⁵⁶Ni masses of 8 SNe IIB, finding that the ⁵⁶Ni masses of SN 1993J, SN 1996cb, SN 2006T, SN 2006el, SN 2008ax, SN 2011dh, SN 2013df, and SN 2016gkg are $0.08 M_{\odot}$, $0.03 M_{\odot}$, $0.08 M_{\odot}$, $0.05 M_{\odot}$, $0.06 M_{\odot}$, $0.09 M_{\odot}$, $0.06 M_{\odot}$, $0.05 M_{\odot}$, respectively (see Table 2 of Afsariardchi et al. 2021). The mean and the median values of the small SNe IIB sample are $0.0625 M_{\odot}$ and $0.06 M_{\odot}$, respectively.

$1.70 M_{\odot}$, $L_1 = 8.71 \times 10^{53}$ erg s $^{-1}$, $t_{\text{tr,fb}} = 14.12$ days, $M_{\text{Ni}} = 0.05 M_{\odot}$, $t_{\text{tr}} = 19.32$ days, $v_{\text{ph1}} = 0.91 \times 10^9$ cm s $^{-1}$, $v_{\text{ph2}} = 0.13 \times 10^9$ cm s $^{-1}$, $T_{\text{f}} = 5235.48$ K, $t_{\text{shift}} = -8.11$ days (the offset of the best-fitting explosion epoch with respect to the explosion epoch adopted by B21 is 7.71 days), $\kappa_{\gamma,\text{Ni}} = 0.20$ cm 2 g $^{-1}$ ($t_{0,\gamma,\text{Ni}} = 145.53$ days), and $\kappa_{\gamma,\text{fb}} = 0.031$ cm 2 g $^{-1}$ ($t_{0,\gamma,\text{fb}} = 58.60$ days). Using Equation 6, ^{56}Ni mass is reduced to $0.03 M_{\odot}$.

Based on the derived parameters, we can infer accretion mass M_{acc} which can be expressed as (Moriya et al. 2018)

$$\eta M_{\text{acc}} c^2 = \int_0^{\infty} L_{\text{input,fb}}(t) dt = 2.5 L_1 t_{\text{tr,fb}}^{-2/3} \quad (9)$$

here, η is the efficiency of converting accretion to input energy. The typical value of η is assumed to be ~ 0.001 (Dexter & Kasen 2013). However, η can also be supposed to be an extreme value of ~ 0.1 (e.g., McKinney 2005; Kumar et al. 2008; Gilkis et al. 2016). Therefore, the range of η value can be $\sim 0.001 - 0.1$. According to the derived values of L_1 and $t_{\text{tr,fb}}$, we find that the accretion mass of SN 2018gk is $0.001 - 0.11 M_{\odot}$.

The problem of the fallback plus ^{56}Ni model is that a decreasing ^{56}Ni mass needs a input function including a time-variant ^{56}Ni mass. However, this effect can be neglected if M_{acc} is very small (e.g., $< 0.01 M_{\odot}$). The accretion mass M_{acc} is only $0.001 - 0.011 M_{\odot}$, if η is $0.01 - 0.1$; the accretion mass can reach about $0.1 M_{\odot}$, which is larger than the initial ^{56}Ni mass ($0.03 M_{\odot}$) we derived, if η is as low as about 0.001 . Therefore, the fallback plus ^{56}Ni model favor a relatively large η , since smaller η would result in a large accreted ^{56}Ni mass higher than the ^{56}Ni mass derived by the model. Therefore, although the fallback plus ^{56}Ni model cannot be excluded, its validity depends on the value of η .

3. THE NIR EXCESSES OF SN 2018GK AND THE PROPERTIES OF POSSIBLE DUST

As pointed out by B21, SN 2018gk show NIR excesses in the H -band flux, which can be due to the strong emission in the H -band or the dust emission. Our multi-band fits also show the H -band excesses at the late-epochs. Furthermore, our blackbody fits for the optical-NIR SEDs at five epochs when at least J - and H - band photometry are available demonstrate that, while the SEDs at first two epochs do not show NIR excesses, the SEDs at the rest three epochs show evident NIR excesses (see Figure 6, the derived parameters are listed in Table 4).

We suppose that the NIR excesses of the SEDs are due to dust emission, and adopt a blackbody plus dust emission model to fit the optical-NIR SEDs of SN 2018gk. The details of the model can be found in Gan et al. (2021), and we suppose that the dust size distribution follow a power law function (see, e.g., Cao et al. 2022 and the references therein). The MCMC method is also used. The free parameters of the model are the dust mass M_d , the dust temperature T_d , the temperature of the SN photosphere T_{ph} , the radius of the SN photosphere R_{ph} . We suppose that the dust might be graphite or silicate. The fits of the model are shown in Figure 7, the derived parameters are listed in Table 5.

We find that the putative dust mass is $\sim 2.9 - 19.4 \times 10^{-3} M_{\odot}$ or $\sim 3.5 - 24.9 \times 10^{-3} M_{\odot}$ for graphitic or silicate dust, the temperature of the dust is $\sim 730 - 850$ or $\sim 780 - 880$ K for the two cases. The derived median values of the dust mass are in the range (a few 10^{-5} to a few $10^{-2} M_{\odot}$) of those of the dust of many SNe (see, e.g., Table 5 of Fox et al. 2013). Moreover, The derived temperature are lower than the evaporation temperatures of silicate ($\sim 1100 - 1500$ K, Laor & Draine 1993; Mattila et al. 2008; Gall et al. 2014) and graphite (~ 1900 K, Stritzinger et al. 2012). These two facts support the assumption that the NIR excesses are from the dust emission.

However, the absence of data in K - band and other bands with longer effective wavelengths at the three epochs prevents us from posing more stringent constraints on the temperature and mass of the putative dust. Especially, the absence of data in bands with longer effective wavelengths would result in a longer derived peak wavelength of the SEDs of the dust emission. A temperature lower than the real value is therefore favorable. Hence, the dust temperature of SN 2018gk we derive can be regarded as the lower limit of the real temperature of the putative dust.

4. DISCUSSION

4.1. The Mass of the Ejecta

The ejecta mass of SN 2018gk derived by the magnetar plus ^{56}Ni model we adopt is $\sim 1.65 M_{\odot}$. According to the analysis of B21, the M_{ZAMS} and the helium core mass just prior to the explosion are $\sim 20 - 25 M_{\odot}$ and $\sim 6 - 8 M_{\odot}$. After removing the putative magnetar with mass being $1.4 M_{\odot}$, the ejecta mass is $\sim 4.6 - 6.6 M_{\odot}$, which is larger than our derived ejecta mass. It seems that the discrepancy between the two value disfavor both the two models.

The contradiction can be eliminated since (1) the magnetar mass can be up to $\sim 2.0 - 2.5 M_{\odot}$, then the the lower limit of the ejecta can be reduced to $3.5 M_{\odot}$; (2) the final masses of the progenitors of SESNe are sensitive to metallicity and the M_{ZAMS} , the SESNe progenitor with $M_{\text{ZAMS}} \sim 18 - 25 M_{\odot}$ might yield ejecta masses of $2.39 - 3.61 M_{\odot}$ (Dessart et al. 2011); (3) the analysis of B21 is based on the single-star evolution model, while the binary-star evolution can reduce the helium core masses of the progenitor masses of SESNe (Yoon et al. 2010); (4) a smaller κ would result in a larger ejecta mass.

Hence, we suggest that the ejecta mass of SN 2018gk derived by the magnetar plus ^{56}Ni model and the model itself are reasonable. The discrepancy between the two values might indicate that the progenitor of SN 2018gk was in a binary system and/or had a low metallicity, or the explosion of SN 2018gk leaved a massive magnetar.

4.2. The Theoretical Bolometric Light Curve, the Temperature Evolution, and the Radius Evolution of SN 2018gk

Based on the best-fitting parameters of the magnetar plus ^{56}Ni model obtained from the multi-band LCs, the theoretical bolometric LC, temperature evolution, and the radius evolution can be reproduced, see Figure 8. For comparison, the same three curves reproduced by the best-fitting parameters of the model adopting photosphere modulus of Nicholl et al. (2017) are also plotted in the same figure.

We find that while the theoretical bolometric LC of both models can fit the the bolometric LC derived by the photometry, temperature and the radius evolution curves reproduced by our model which use a generalized photosphere modulus can better match those derived by the photometry. This indicate the photosphere velocity have decreased before the temperature reached the temperature floor (T_f), and demonstrate the necessity of generalizing the photosphere modulus.

We find the rise time of the bolometric LC of SN 2018gk reproduced by the best-fitting parameters of the magnetar plus ^{56}Ni model is ~ 13.2 days which is significantly longer than the rise time ($\lesssim 5$ days, see Figure 14 of B21) of the bolometric LC reproduced by B21 using the magnetar plus ^{56}Ni model. The peak luminosity of the bolometric LC reproduced is $\sim 4.35 \times 10^{43} \text{ erg s}^{-1}$, which is half of the peak luminosity ($\sim 10^{44} \text{ erg s}^{-1}$) derived by B21 using the magnetar plus ^{56}Ni model. Our derived peak luminosity of the bolometric LC of SN 2018gk also suggests that SN 2018gk is one of luminous SNe which bridges the gap between SLSNe (whose peak bolometric luminosity are $\gtrsim 7 \times 10^{43} \text{ erg s}^{-1}$, Gal-Yam 2012) and normal-luminosity SNe.

5. CONCLUSIONS

SN 2018gk is a luminous SN IIb whose peak luminosity is between those of SLSNe and normal SNe. In this paper, we perform a comprehensive study for the physical properties of SN 2018gk. Based on the SED fits, we find that the early-time photospheric velocity vary from a larger value to a smaller value before the photosphere reach a temperature floor. We generalize the photosphere modulus by assuming that the the photospheric velocity of SN 2018gk has two different values at two time episodes before reaching the photosphere reach the temperature floor.

By incorporating the generalized photosphere modulus to different energy source models, we fit the multi-band LCs of SN 2018gk. We conclude the ^{56}Ni model cannot fit the multi-band LCs of SN 2018gk, since the derived ^{56}Ni mass ($\sim 0.9 M_{\odot}$) is significantly larger than the ejecta mass ($\sim 0.10 M_{\odot}$) if the ^{56}Ni model is adopted.

In contrast, we find that the magnetar plus ^{56}Ni and the fallback plus ^{56}Ni models can fit the multi-band LCs of SN 2018gk. It should be pointed out that, however, the validity of the fallback plus ^{56}Ni model depends on the value of η , and favors a relatively large η . Hence, we favor the magnetar plus ^{56}Ni model, though the fallback plus ^{56}Ni model cannot be excluded.

The ^{56}Ni mass ($0.05 M_{\odot}$) derived here by using the magnetar plus ^{56}Ni model is significantly lower than that ($\sim 0.9 M_{\odot}$) required by the ^{56}Ni model adopted here, indicating that the magnetar can significantly reduce ^{56}Ni mass required to power the LCs of SN 2018gk. The derived ^{56}Ni mass of the magnetar plus ^{56}Ni model is about 1/6 of the value ($\sim 0.3 M_{\odot}$) derived by B21 using the same scenario, and comparable to the ^{56}Ni masses of typical SNe IIb. Moreover, our derived ^{56}Ni mass is lower than the upper limit ($0.2 M_{\odot}$) of the value of the ^{56}Ni mass can be synthesized by the neutrino-powered CCSNe.

The value of P_0 (10.42 ms) derived by the magnetar plus ^{56}Ni model we adopt is about 8 times that (1.2 ms) derived by B21; the derived value of B ($6.52 \times 10^{14} \text{ G}$) is about 1/6 of that ($4 \times 10^{15} \text{ G}$) derived by B21. A larger P_0 usually results in a lower input power and a lower peak luminosity. In general, magnetars with $P_0 \sim 1 - 5 \text{ ms}$ and $B \sim 10^{14} - 10^{15} \text{ G}$ would power SLSNe (see, e.g., Nicholl et al. 2017; Liu et al. 2017), while magnetar with $P_0 \sim 5 - 20 \text{ ms}$ and $B \sim 10^{13} - 10^{15} \text{ G}$ would power luminous SNe (see, e.g., Wang et al. 2015; Gomez et al. 2022) with rare

exceptions. Hence, we suggest our derived parameters of the magnetar supposed to power the LCs of SN 2018gk are reasonable, since SN 2018gk is a luminous SN rather than a SLSN.

Therefore, we suggest that the magnetar plus a moderate amount of ^{56}Ni can be responsible for the luminous LCs of SN 2018gk. To our knowledge, other luminous SNe I Ib requiring central engines (plus ^{56}Ni) to account for their LCs are PTF10hgi and DES14X2fna. So SN 2018gk might be one of rare SNe I Ib mainly powered by a central engine.

Based on the best-fitting parameters of the magnetar plus ^{56}Ni model, we plot the bolometric LC, the photospheric temperature evolution, and the photospheric radius evolution of SN 2018gk, and compare them with those from the SED fits. The peak of the theoretical bolometric LC of SN 2018gk is $\sim 4.35 \times 10^{43} \text{ erg s}^{-1}$ which is below the fiducial threshold of SLSNe ($\lesssim 7 \times 10^{43} \text{ erg s}^{-1}$; Gal-Yam (2012)) and the peak luminosity ($\sim 10^{44} \text{ erg s}^{-1}$ derived by B21). The rise time of the theoretical bolometric LC of SN 2018gk is ~ 13.2 days which is comparable to those of many SESNe.

Moreover, we find that the theoretical evolution of the temperature and the radius of the photosphere are well matched by those from SED fits. For comparison, we also plot the theoretical evolution of the temperature and the radius of the photosphere based on the simple photosphere modulus that assume the photosphere velocity are constants before the temperature floor are reached deviated from those from the SED fits from 30–60 after the derived explosion date. We suggests that the conventional photosphere modulus cannot describe the early-time photospheric evolution of a fraction of SNe and generalized photosphere modulus would be considered as alternative ones.

Finally, we find that the blackbody plus dust emission model can account for the NIR excesses of the SEDs of SN 2018gk at some epochs. The derived masses of the dust are $\sim 2.9 - 19.4 \times 10^{-3} M_{\odot}$ ($\sim 3.5 - 24.9 \times 10^{-3} M_{\odot}$) for graphite (silicate) grains, respectively; the derived temperatures of the dust of the SN are $\sim 730 - 850$ ($\sim 780 - 880$) K for graphite (silicate) grains, respectively. Due to the absence of photometry at K -band and other bands with longer effective wavelengths, the real parameters cannot be well constrained, and the derived dust temperature might be the lower limit of the real temperature of the dust.

- 1 We thank the anonymous referee for helpful comments and suggestions that have allowed us to improve this manuscript.
- 2 Wang Tao thank Jia-Wei Li (李佳伟), Shuai-Cong Wang (王帅聪), Deng-Wang Shi (石登旺), Song-Yao Bai (白松瑶)
- 3, and Jing-Yao Li (李京瑶) for helpful discussion. This work is supported by National Natural Science Foundation of
- 4 China (grant Nos. 11963001, 12133003).

REFERENCES

- Afsariardchi, N., Drout, M. R., Khatami, D. K., et al. 2021, *ApJ*, 918, 89
- Arnett, W. D. 1982, *ApJ*, 253, 785
- Bose, S., Dong, S., Kochanek, C. S., et al., 2021, *MNRAS*, 503, 3472
- Brimacombe J., Stone G., Stanek K. Z., 2018, *Transient Name Serv. Discovery Rep.*, 2018-54, 1
- Cao, X. M., Wang, S. Q., Gan, W. P., et al. 2022, *arXiv:2210.04115*
- Cappellaro, E., Mazzali, P. A., Benetti, S., et al. 1997, *A&A*, 328, 203
- Chatzopoulos, E., Wheeler, J. C., & Vinko, J. 2009, *ApJ*, 704, 1251
- Chatzopoulos, E., Wheeler, J. C., & Vinko, J. 2012, *ApJ*, 746, 121
- Clocchiatti, A., Wheeler, J. C., Benetti, S., & Frueh, M. 1996, *ApJ*, 459, 547
- De Cia, A., Gal-Yam, A., Rubin, A., et al. 2018, *ApJ*, 860, 100
- Dessart, L., Hillier, D. J., Livne, E., et al. 2011, *MNRAS*, 414, 2985
- Dexter, J. & Kasen, D. 2013, *ApJ*, 772, 30
- Ertl, T., Woosley, S. E., Sukhbold, T., et al. 2020, *ApJ*, 890, 51
- Filippenko, A. V. 1988, *AJ*, 96, 1941
- Filippenko, A. V. 1997, *ARA&A*, 35, 309
- Foreman-Mackey, D., Hogg, D. W., Lang, D., & Goodman, J. 2013, *PASP*, 125, 306
- Fox, O. D., Filippenko, A. V., Skrutskie, M. F., et al. 2013, *AJ*, 146, 2
- Gagliano, A., Izzo, L., Kilpatrick, C. D., et al. 2022, *ApJ*, 924, 55
- Gall, C., Hjorth, J., Watson, D., et al. 2014, *Nature*, 511, 326
- Gal-Yam, A. 2012, *Science*, 337, 927
- Gan, W. P., Wang, S. Q., & Liang, E. W. 2021, *ApJ*, 914, 125.
- Gilkis, A., Soker, N., & Papish, O. 2016, *ApJ*, 826, 178
- Gomez, S., Berger, E., Nicholl, M., et al. 2022, *arXiv:2204.08486*
- Grayling, M., Gutiérrez, C. P., Sullivan, M., et al. 2021, *MNRAS*, 505, 3950
- Inserra, C., Smartt, S. J., Jerkstrand, A., et al. 2013, *ApJ*, 770, 128
- Kasen D., Bildsten L., 2010, *ApJ*, 717, 245
- Katz B., Kushnir D., Dong S., 2013, preprint (*arXiv:1301.6766*)
- Khatami, D. K., & Kasen, D. N. 2019, *ApJ*, 878, 56
- Kochanek, C. S., Shappee, B. J., Stanek, K. Z., et al. 2017, *PASP*, 129, 104502
- Kumar, P., Narayan, R., & Johnson, J. L. 2008, *MNRAS*, 388, 1729
- Laor, A., & Draine, B. T. 1993, *ApJ*, 402, 441
- Liu, L. D., Wang, S. Q., Wang, L. J., et al. 2017, *ApJ*, 842, 26
- Maeda, K., Mazzali, P. A., Deng, J., et al. 2003, *ApJ*, 593, 931
- Maeda, K., Mazzali, P. A., Deng, J., et al. 2003, *ApJ*, 593, 931
- Mattila, S., Meikle, W. P. S., Lundqvist, P., et al. 2008, *MNRAS*, 389, 141
- Mazzali, P. A., Iwamoto, K., & Nomoto, K. 2000, *ApJ*, 545, 407
- Mazzali, P. A., Sauer, D. N., Pian, E., et al. 2017, *MNRAS*, 469, 2498
- McKinney, J. C. 2005, *ApJL*, 630, L5
- Milne, P. A., The, L.-S., & Leising, M. D. 1999, *ApJS*, 124, 503
- Moriya, T. J., Nicholl, M., & Guillochon, J. 2018, *ApJ*, 867, 113
- Nagy, A. P. & Vinkó, J. 2016, *A&A*, 589, A53
- Nicholl, M., Guillochon, J., & Berger, E. 2017, *ApJ*, 850, 55
- Planck Collaboration, 2014, *A&A*, 571, A16
- Podsiadlowski, P., Joss, P. C., & Hsu, J. J. L. 1992, *ApJ*, 391, 246
- Prajs, S., Sullivan, M., Smith, M., et al. 2017, *MNRAS*, 464, 3568
- Quimby, R. M., De Cia, A., Gal-Yam, A., et al. 2018, *ApJ*, 855, 2
- Schlafly, E. F., & Finkbeiner, D. P. 2011, *ApJ*, 737, 103
- SDSS Collaboration, 2017, *ApJS*, 233, 25
- Shappee, B. J., Prieto, J. L., Grupe, D., et al. 2014, *ApJ*, 788, 48
- Soker, N. & Kaplan, N. 2021, *ApJ*, 907, 120
- Sravan, N., Marchant, P., & Kalogera, V. 2019, *ApJ*, 885, 130
- Stritzinger, M., Taddia, F., Fransson, C., et al. 2012, *ApJ*, 756, 173
- Sukhbold, T., Ertl, T., Woosley, S. E., et al. 2016, *ApJ*, 821, 38
- Sutherland, P. G. & Wheeler, J. C. 1984, *ApJ*, 280, 282
- Swartz, D. A., Sutherland, P. G., & Harkness, R. P. 1995, *ApJ*, 446, 766
- Valenti, S., Benetti, S., Cappellaro, E., et al. 2008, *MNRAS*, 383, 1485
- Wang, S. Q., & Gan, W. P. 2022, *ApJ*, 928, 114

Wang, S. Q., Wang, L. J., Dai, Z. G., & Wu, X. F. 2015, ApJ, 807, 147

Wang, S. Q., Wang, L. J., Dai, Z. G., et al. 2015, ApJ, 799, 107

Wang, L. J., Wang, S. Q., Dai, Z. G., et al. 2016, ApJ, 821, 22

Woosley, S. E., Heger, A., & Weaver, T. A. 2002, Reviews of Modern Physics, 74, 1015

Woosley, S. E. 2010, ApJL, 719, L204

Yan, L., Perley, D. A., Schulze, S. et al. 2020, ApJL, 902, L8

Yoon, S.-C., Woosley, S. E., & Langer, N. 2010, ApJ, 725, 940

Yoon, S.-C., Dessart, L., & Clocchiatti, A. 2017, ApJ, 840, 10

Table 1. The Definitions, the units, the prior, the medians, 1- σ bounds, and the best-fitting values for the parameters of the ^{56}Ni model. The values of χ^2/dof (reduced χ^2 , dof=degree of freedom) are also presented.

Parameters	Definition	Unit	Prior	Best fit	Median
M_{ej}	The ejecta mass	M_{\odot}	[0.1, 50]	0.10	$0.10^{+0.00}_{-0.00}$
t_{tr}	The photospheric velocity transition time	day	[0, 100]	14.02	$14.03^{+0.11}_{-0.11}$
v_{ph1}	The first episode photospheric velocity	10^9 cm s^{-1}	[0, 5]	1.52	$1.52^{+0.01}_{-0.01}$
v_{ph2}	The second episode photospheric velocity	10^9 cm s^{-1}	[0, 5]	0.16	$0.16^{+0.01}_{-0.01}$
M_{Ni}	The ^{56}Ni mass	M_{\odot}	[0.0, 4]	1.59	$1.58^{+0.01}_{-0.01}$
$\log \kappa_{\gamma, \text{Ni}}$	The γ -ray opacity of ^{56}Ni -cascade-decay	$\text{cm}^2 \text{g}^{-1}$	[-1.568, 4]	-0.45	$-0.45^{+0.01}_{-0.01}$
κ_{e^+}	The positron opacity	$\text{cm}^2 \text{g}^{-1}$	[4, 14]	4.00	$4.00^{+0.01}_{-0.00}$
T_{f}	The temperature floor of the photosphere	K	[1000, 10^4]	4921.90	$4920.83^{+15.20}_{-15.00}$
t_{shift}	The explosion time relative to the first data	day	[-20, 0]	-1.76	$-1.78^{+0.05}_{-0.05}$
λ_{CF}	The cutoff wavelength	\AA	[0, 4000]	2005.60	$2014.99^{+15.44}_{-10.22}$
β'	The dimensionless free parameter		[0, 10]	4.47	$3.61^{+4.21}_{-3.40}$
χ^2/dof				9.30	9.30

Table 2. The Definitions, the units, the prior, the medians, 1- σ bounds, and the best-fitting values for the parameters of the magnetar plus ^{56}Ni model. The values of χ^2/dof (reduced χ^2 , dof=degree of freedom) are also presented.

Parameters	Definition	Unit	Prior	Best fit	Median
M_{ej}	The ejecta mass	M_{\odot}	[0.1, 50]	1.65	$1.61^{+0.08}_{-0.08}$
P_0	The initial period of the magnetar	ms	[0.8, 50]	10.42	$10.43^{+0.03}_{-0.03}$
B	The magnetic field strength of the magnetar	10^{14} G	[0.1, 100]	6.52	$6.48^{+0.11}_{-0.11}$
t_{tr}	The photospheric velocity transition time	day	[0, 100]	17.15	$17.01^{+0.11}_{-0.11}$
v_{ph1}	The first episode photospheric velocity	10^9 cm s $^{-1}$	[0, 5]	1.07	$1.07^{+0.01}_{-0.01}$
v_{ph2}	The second episode photospheric velocity	10^9 cm s $^{-1}$	[0, 5]	0.11	$0.11^{+0.01}_{-0.01}$
M_{Ni}	The ^{56}Ni mass	M_{\odot}	[0, $0.2M_{\text{ej}}$]	0.08	$0.08^{+0.00}_{-0.00}$
$\log \kappa_{\gamma, \text{mag}}$	The γ -ray opacity of magnetar photons	cm 2 g $^{-1}$	[-2, 4]	-1.55	$-1.55^{+0.02}_{-0.02}$
$\log \kappa_{\gamma, \text{Ni}}$	The γ -ray opacity of ^{56}Ni -cascade-decay photons	cm 2 g $^{-1}$	[-1.568, 4]	-0.72	$-0.72^{+0.04}_{-0.04}$
κ_{e^+}	The positron opacity	cm 2 g $^{-1}$	[4, 14]	7.02	$8.95^{+3.43}_{-3.35}$
T_{f}	The temperature floor of the photosphere	K	[1000, 10^4]	5254.04	$5244.27^{+17.10}_{-17.11}$
t_{shift}	The explosion time relative to the first data	day	[-20, 0]	-6.35	$-6.29^{+0.07}_{-0.06}$
λ_{CF}	The cutoff wavelength	Å	[0, 4000]	2007.99	$2019.53^{+1302.88}_{-13.33}$
β'	The dimensionless free parameter		[0, 10]	3.82	$1.95^{+5.33}_{-1.92}$
χ^2/dof				6.08	6.08

Table 3. The Definitions, the units, the prior, the medians, 1- σ bounds, and the best-fitting values for the parameters of the fallback plus ^{56}Ni model. The values of χ^2/dof (reduced χ^2 , dof=degree of freedom) are also presented.

Parameters	Definition	Unit	Prior	Best fit	Median
M_{ej}	The ejecta mass	M_{\odot}	[0.1, 50]	1.70	$1.66^{+0.15}_{-0.17}$
$\log L_1$	The constant	erg s^{-1}	[48, 58]	53.94	$53.94^{+0.00}_{-0.01}$
$\log t_{\text{tr,fb}}$	The transition time	day	[-3, 3]	1.15	$1.15^{+0.01}_{-0.01}$
t_{tr}	The photospheric velocity transition time	day	[0, 100]	19.32	$19.04^{+0.32}_{-0.45}$
v_{ph1}	The first episode photospheric velocity	10^9 cm s^{-1}	[0, 5]	0.91	$0.91^{+0.01}_{-0.01}$
v_{ph2}	The second episode photospheric velocity	10^9 cm s^{-1}	[0, 5]	0.13	$0.14^{+0.02}_{-0.02}$
M_{Ni}	The ^{56}Ni mass	M_{\odot}	[0, $0.2M_{\text{ej}}$]	0.05	$0.05^{+0.00}_{-0.00}$
$\log \kappa_{\gamma,\text{fb}}$	The γ -ray opacity of fallback photons	cm^2g^{-1}	[-2, 4]	-1.58	$-1.56^{+0.04}_{-0.03}$
$\log \kappa_{\gamma,\text{Ni}}$	The γ -ray opacity of ^{56}Ni -cascade-decay photons	cm^2g^{-1}	[-1.568, 4]	-0.79	$-0.75^{+0.06}_{-0.07}$
$\kappa_{\text{e}+}$	The positron opacity	cm^2g^{-1}	[4, 14]	12.11	$9.00^{+3.43}_{-3.45}$
T_{f}	The temperature floor of the photosphere	K	[1000, 10^4]	5235.48	$5227.37^{+17.13}_{-17.03}$
t_{shift}	The explosion time relative to the first data	day	[-20, 0]	-8.11	$-8.07^{+0.13}_{-0.10}$
λ_{CF}	The cutoff wavelength	\AA	[0, 4000]	3995.45	$3980.84^{+14.25}_{-28.87}$
β'	The dimensionless free parameter		[0, 10]	0.30	$0.30^{+0.03}_{-0.03}$
χ^2/dof				6.38	6.39

Table 4. The best-fitting parameters (the temperature of the photosphere T_{ph} , the radius of the photosphere R_{ph}) of the blackbody model for the SEDs of SN 2018gk.

Phase ^a	T_{ph}	R_{ph}	χ^2/dof
(days)	(10^3 K)	(10^{15} cm)	
56.92	$5689.72^{+100.62}_{-93.12}$	$1.95^{+0.07}_{-0.07}$	1.51
74.75	$5604.40^{+64.62}_{-63.81}$	$1.48^{+0.03}_{-0.03}$	4.82
120.20	$5238.48^{+83.88}_{-81.47}$	$0.90^{+0.03}_{-0.03}$	12.33
137.83	$5479.72^{+126.27}_{-114.47}$	$0.67^{+0.03}_{-0.03}$	9.12
161.92	$5477.06^{+182.17}_{-164.62}$	$0.52^{+0.04}_{-0.04}$	4.44

^a All the phases are relative to the date of the first data which is MJD 58131. All epochs are transformed to the rest-frame ones.

Table 5. The best-fitting parameters (the temperature of the photosphere T_{ph} , the radius of the photosphere R_{ph} , the temperature of the dust shell T_{d} , and the mass of the dust shell M_{d}) of the blackbody plus graphite (silicate) model for the SEDs of SN 2018gk.

Phase ^a (days)	Blackbody plus Graphite					Blackbody plus Silicate				
	T_{ph} (K)	R_{ph} (10^{15} cm)	T_{d} (10^3 K)	M_{d} (10^{-3} M_{\odot})	χ^2/dof	T_{ph} (K)	R_{ph} (10^{15} cm)	T_{d} (10^3 K)	M_{d} (10^{-3} M_{\odot})	χ^2/dof
120.2d	$5577.90^{+111.00}_{-105.84}$	$0.77^{+0.03}_{-0.03}$	$730.97^{+114.12}_{-61.60}$	$19.48^{+43.06}_{-15.93}$	5.89	$5578.90^{+113.03}_{-106.33}$	$0.78^{+0.04}_{-0.03}$	$778.38^{+111.61}_{-59.92}$	$24.97^{+42.12}_{-19.36}$	5.95
137.83d	$5662.40^{+132.20}_{-125.73}$	$0.62^{+0.03}_{-0.03}$	$782.24^{+209.56}_{-114.32}$	$5.03^{+33.11}_{-4.64}$	6.78	$5663.89^{+136.42}_{-127.31}$	$0.62^{+0.03}_{-0.03}$	$829.07^{+220.23}_{-115.19}$	$6.99^{+36.10}_{-6.37}$	6.82
161.92d	$6033.30^{+294.80}_{-256.57}$	$0.41^{+0.05}_{-0.04}$	$846.32^{+249.12}_{-157.24}$	$2.09^{+22.43}_{-1.92}$	1.09	$6040.78^{+304.24}_{-254.25}$	$0.41^{+0.05}_{-0.04}$	$886.62^{+257.65}_{-156.72}$	$3.55^{+28.87}_{-3.22}$	1.10

^a All the phases are relative to the date of the first data which is MJD 58131. All epochs are transformed to the rest-frame ones.

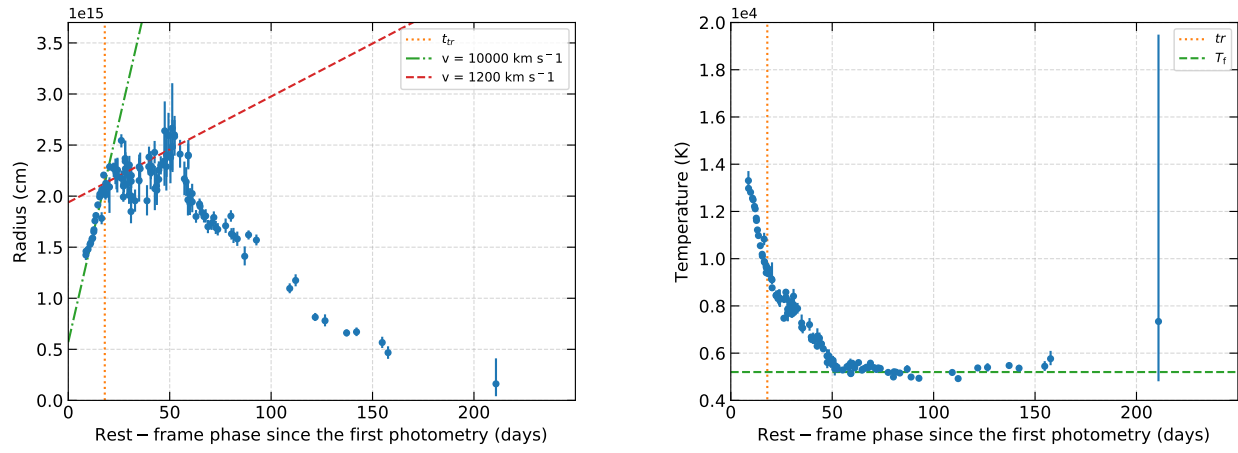


Figure 1. The radius evolution and the temperature evolution derived by the fits for the SEDs at different epochs.

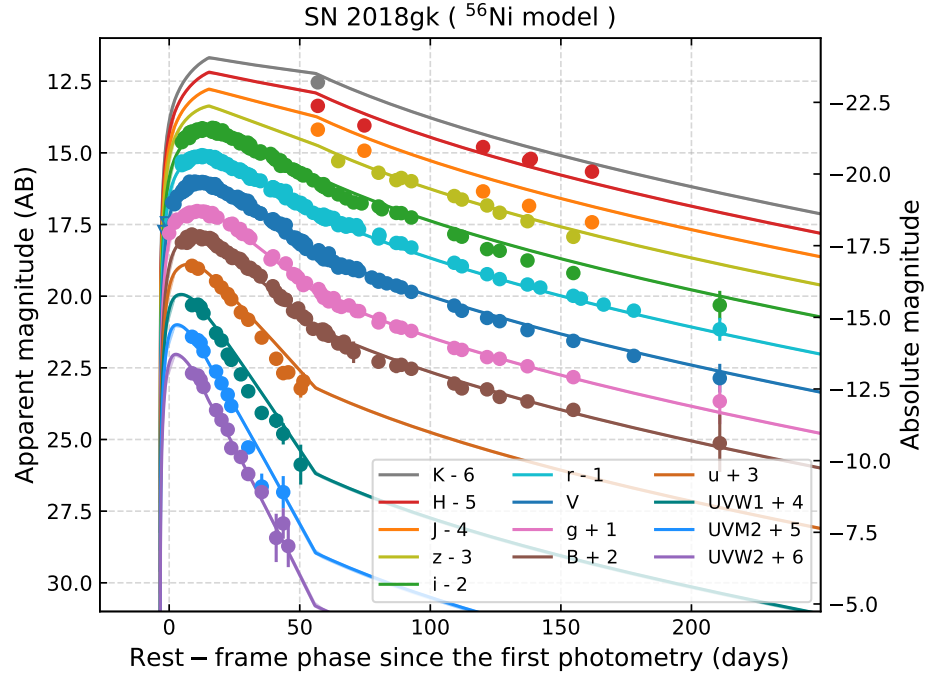


Figure 2. The best fits (the solid curves) of the multi-band LCs of SN 2018gk using the ^{56}Ni model. The shaded regions indicate $1\text{-}\sigma$ bounds of the parameters. The data are from Table 1 of B21, triangles represent upper limits.

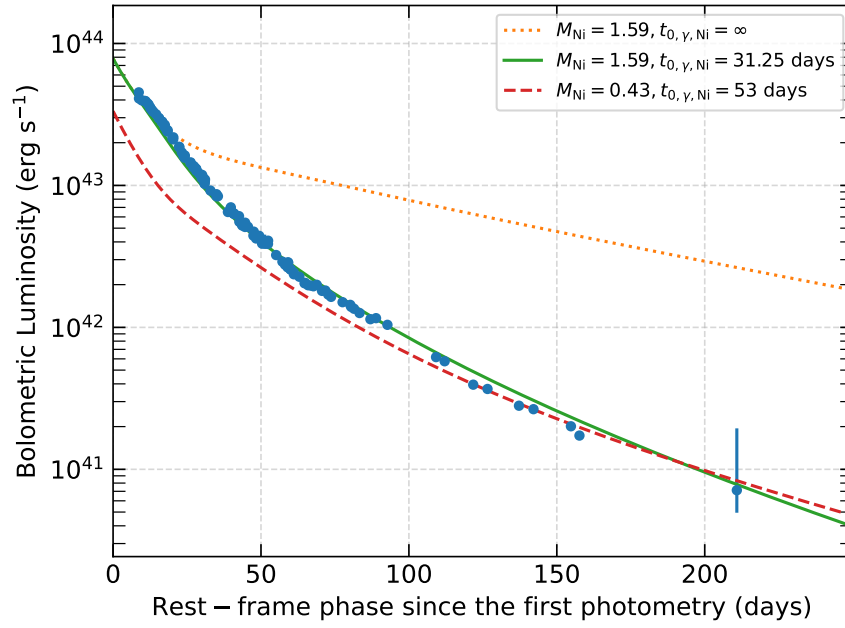


Figure 3. Our synthesized bolometric LC of SN 2018gk (blue points), the power injection function curve derived from the parameters of B21 ($M_{\text{Ni}} = 0.43M_{\odot}$, $t_{0,\gamma,\text{Ni}} = 53$ days, $t_{\text{shift}} = -0.4$ days, the red dashed line), as well as the power injection function curve derived from our parameters ($M_{\text{Ni}} = 1.59 M_{\odot}$, $t_{0,\gamma,\text{Ni}} = 31.25$ days, $t_{\text{shift}} = -1.76$ days, the green solid line). For comparison, the curve derived from $M_{\text{Ni}} = 1.59 M_{\odot}$ and a infinite $t_{0,\gamma,\text{Ni}}$ is also plotted (the orange dotted line).

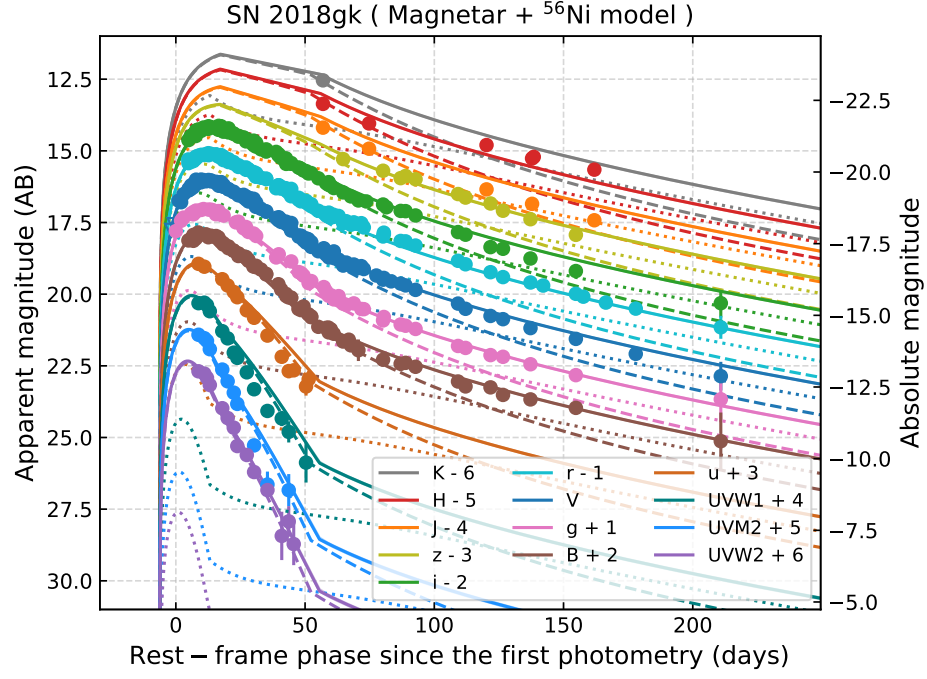


Figure 4. The best fits (the solid curves) of the multi-band LCs of SN 2018gk using the magnetar plus ^{56}Ni . The shaded regions indicate $1\text{-}\sigma$ bounds of the parameters. The dotted lines and dashed lines are the LCs powered by the ^{56}Ni and the magnetar, respectively. The data are from Table 1 of B21, triangles represent upper limits.

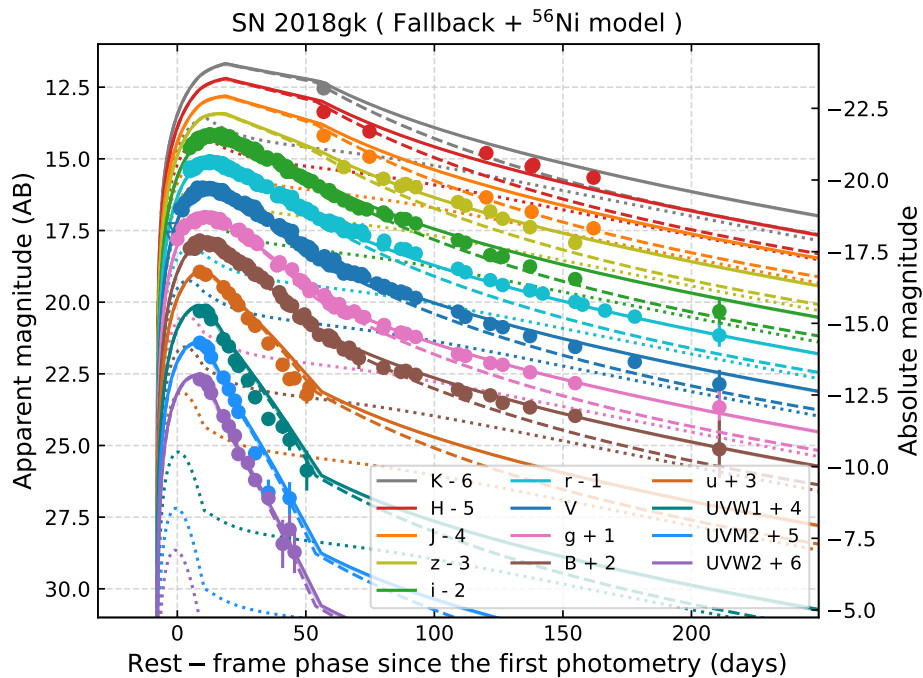


Figure 5. The best fits (the solid curves) of the multi-band LCs of SN 2018gk using the fallback plus ^{56}Ni model. The shaded regions indicate $1\text{-}\sigma$ bounds of the parameters. The dotted lines and dashed lines are the LCs powered by the ^{56}Ni and the fallback, respectively. The data are from Table 1 of B21, triangles represent upper limits.

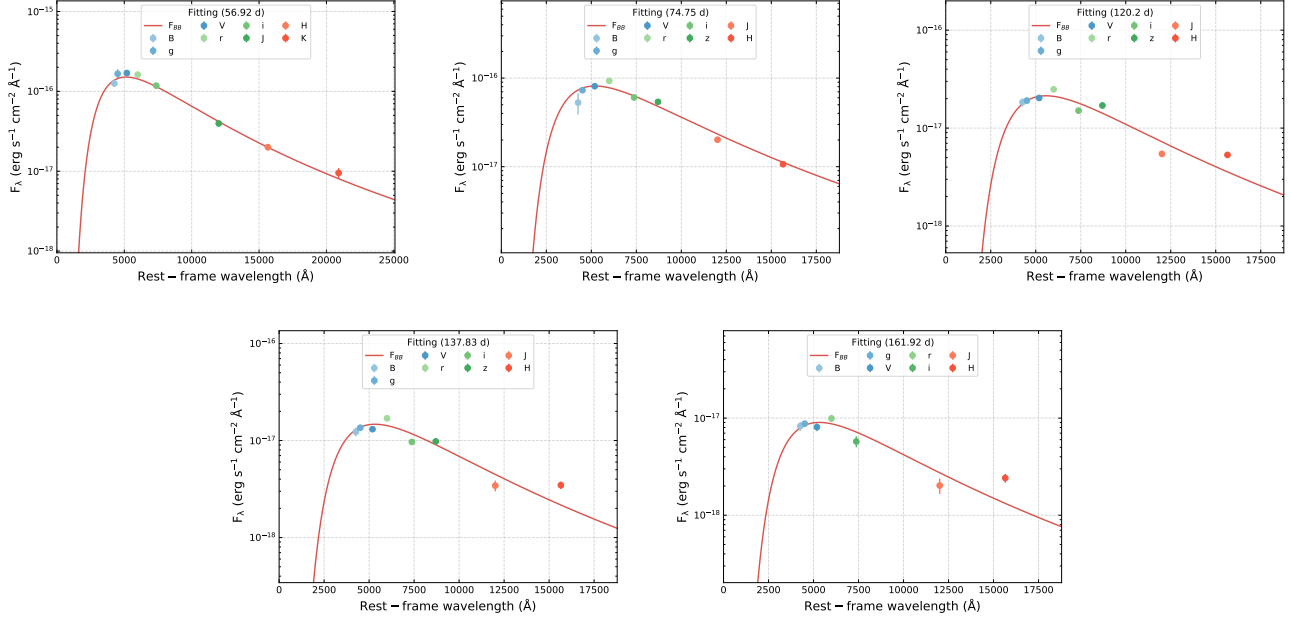


Figure 6. The blackbody fits for SEDs of SN 2018gk at five epochs.

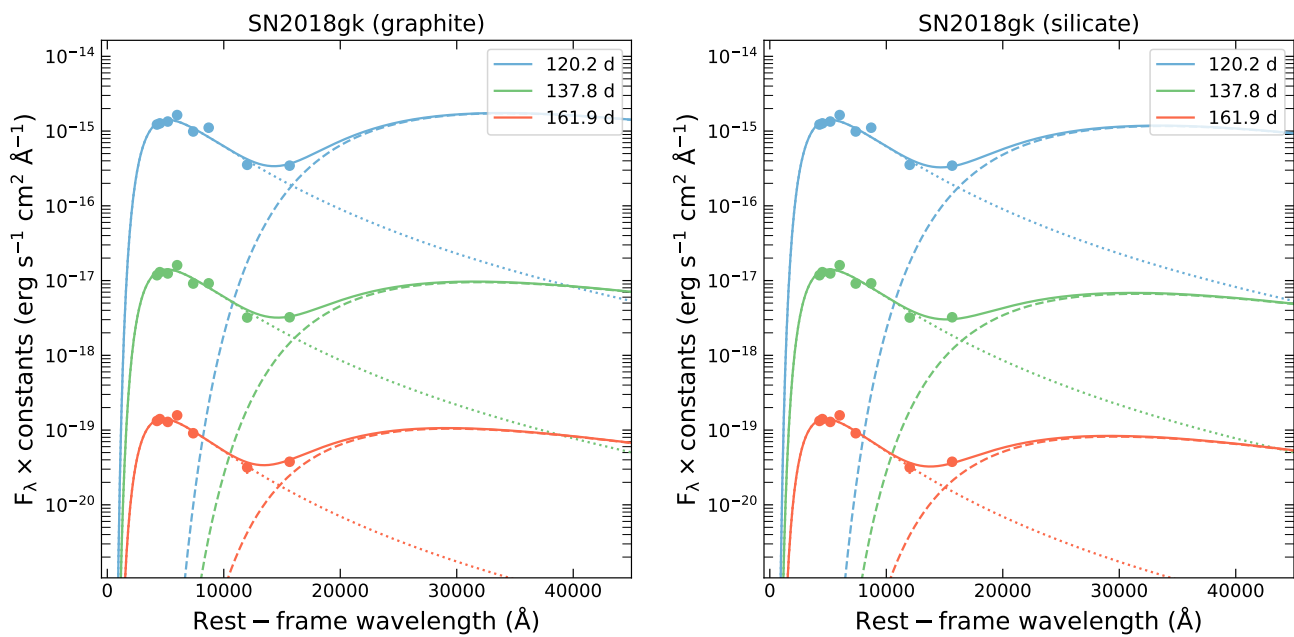


Figure 7. The blackbody plus dust emission model fits for SEDs of SN 2018gk at three epochs. The graphite (left panel) and silicate (right panel) dust are adopted. The dotted, dashed, and solid lines represent the flux of the photospheres, the dust, and the sum of the two components, respectively.

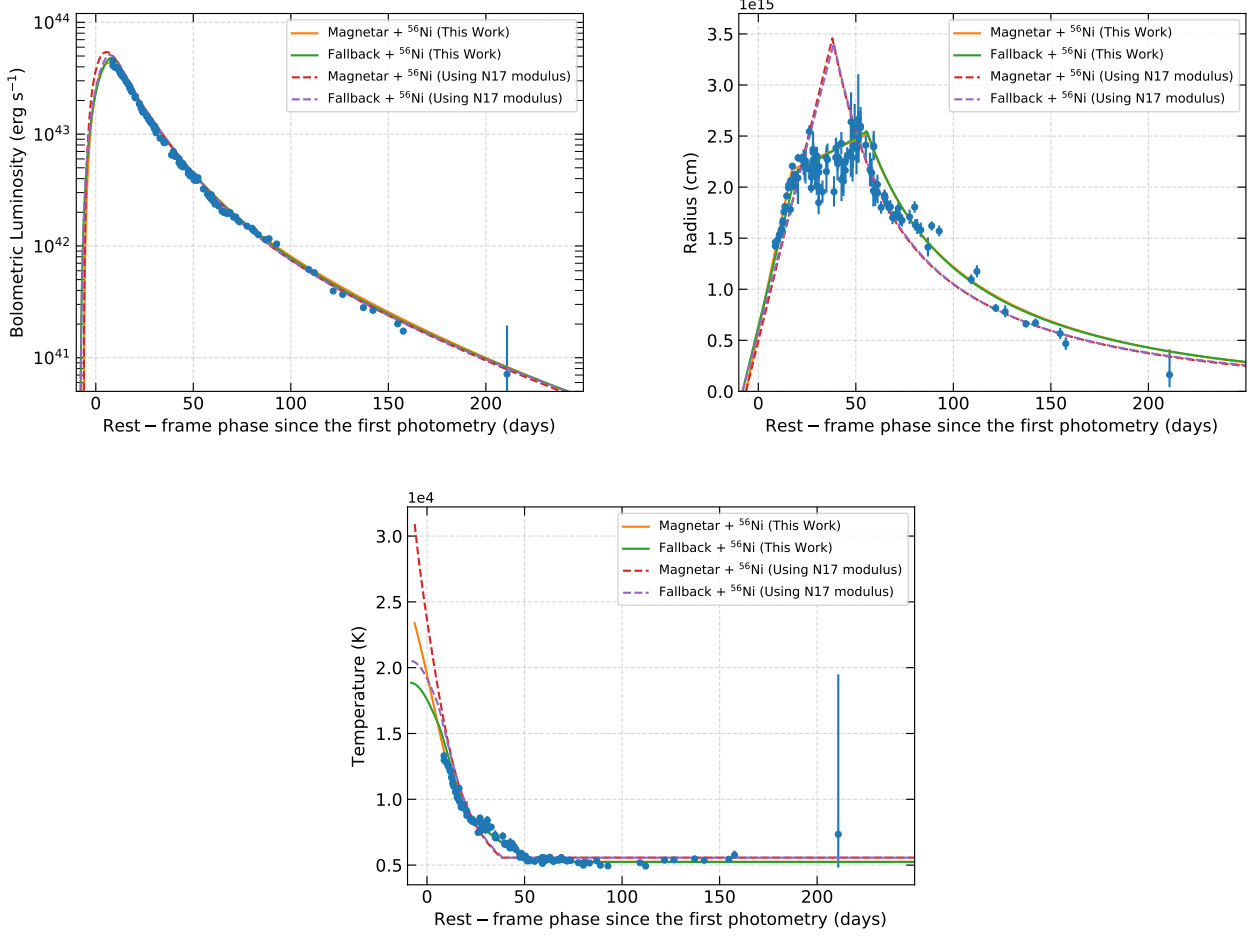


Figure 8. The bolometric LCs (top-left panel), the radius evolution (top-right panel), and the temperature evolution (the bottom panel) reproduced by the best-fitting parameters of the magnetar plus ⁵⁶Ni model (orange solid lines) and fallback plus ⁵⁶Ni model (green solid lines), and the bolometric LCs, the radius evolution, and the temperature evolution derived from the observations (blue filled points). For comparison, the bolometric LCs, the radius evolution, and the temperature evolution using the photosphere modulus of Nicholl et al. (2017) (N17) are also presented (red and purple dashed lines). The t_{shift} values of our magnetar plus ⁵⁶Ni and fallback plus ⁵⁶Ni models are -6.35 days and -8.11 days, respectively; the t_{shift} values of the magnetar plus ⁵⁶Ni and fallback plus ⁵⁶Ni model using N17's the photosphere modulus are -6.30 days and -8.01 days, respectively.

APPENDIX

Figures A1, A2, and A3 present the corner plots of the ^{56}Ni model, the magnetar plus ^{56}Ni model, and the fallback plus ^{56}Ni model, respectively.

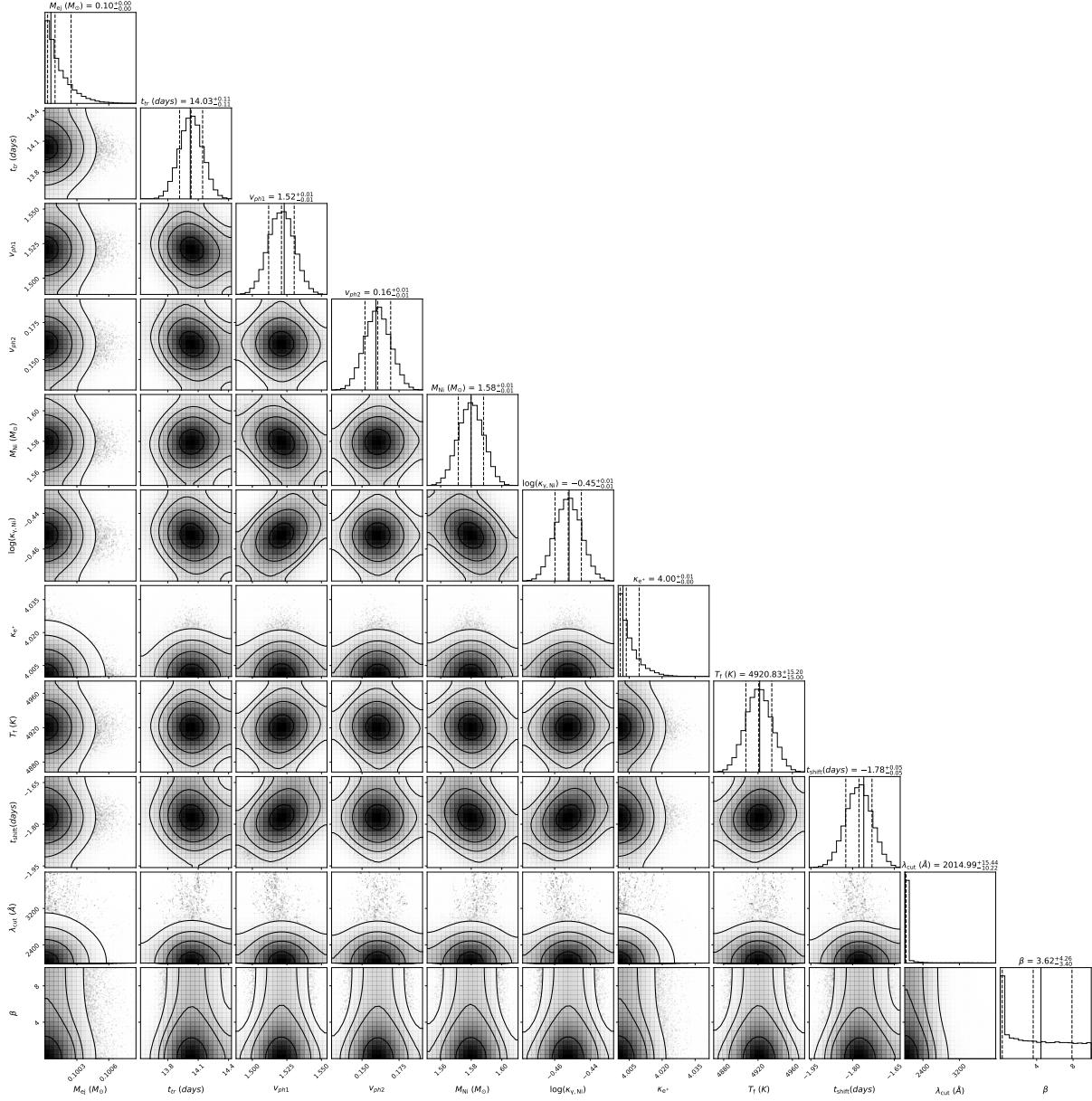


Figure A1. The corner plot of the ^{56}Ni model. The solid vertical lines represent the best-fitting parameters, while the dashed vertical lines represent the medians and the 1- σ bounds of the parameters.

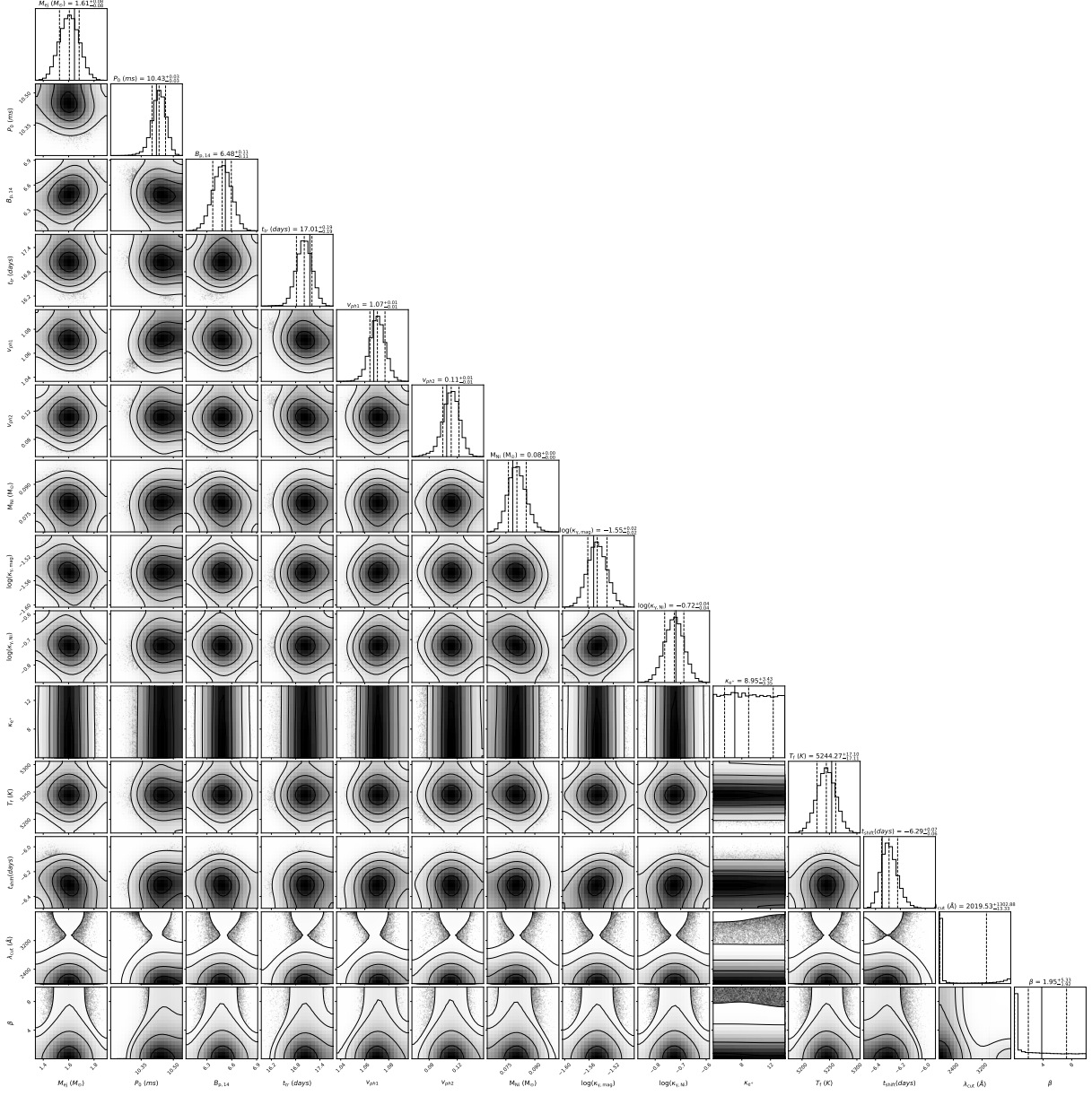


Figure A2. The corner plot of the magnetar plus ^{56}Ni model. The solid vertical lines represent the best-fitting parameters, while the dashed vertical lines represent the medians and the $1\text{-}\sigma$ bounds of the parameters.

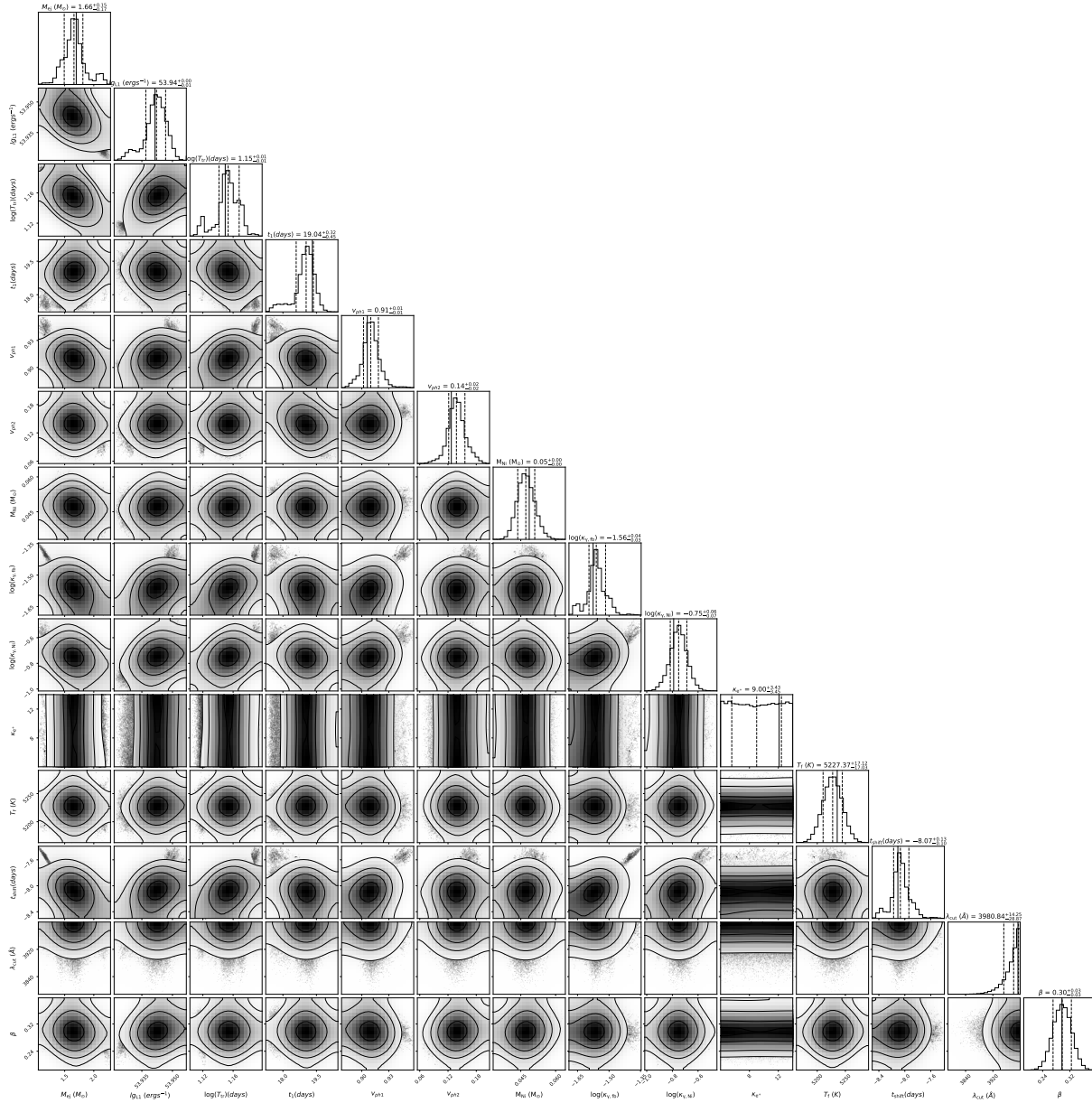


Figure A3. The corner plot of the fallback plus ^{56}Ni model. The solid vertical lines represent the best-fitting parameters, while the dashed vertical lines represent the medians and the 1- σ bounds of the parameters.